J. Fluid Mech. (2021), *vol*. 911, A2, doi:10.1017/jfm.2020.993

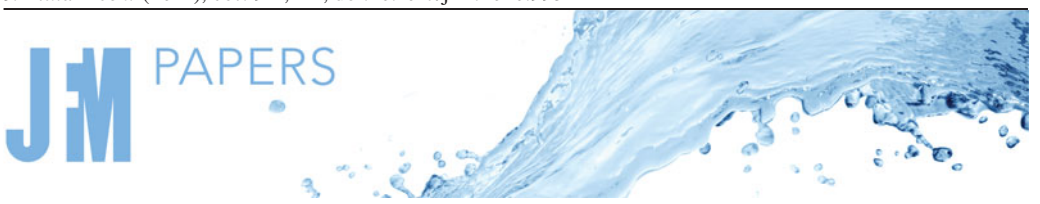

Large-scale coherent structures in compressible turbulent boundary layers

Matthew Bross[1],†, **Sven Scharnowski**[1] **and Christian J. Kähler**[1]

[1]Institute of Fluid Mechanics and Aerodynamics, Universität der Bundeswehr München, 85577 Neubiberg, Germany

(Received 21 January 2020; revised 11 July 2020; accepted 7 November 2020)

The presence of large-scale coherent structures in various wall bounded turbulent flows, often called superstructures in turbulent boundary layers (TBLs), has been of great interest in recent years. These meandering high- and low-momentum structures can extend up to several boundary layer thicknesses in the streamwise direction and contain a relatively large portion of the layer's turbulent kinetic energy. Therefore, studying these features is important for understanding the overall dynamics of turbulent boundary layers and for the development of flow control strategies or near-wall flow modifications. However, compared to the extensive number of incompressible investigations, much less is known about the structural characteristics for compressible turbulent boundary layer flows. Therefore, in this investigation turbulent boundary layers developing on a flat plate with zero pressure gradient (ZPG) over a range of Reynolds numbers and Mach numbers are considered in order to examine the effect of compressibility on superstructures. More specifically, measurements are performed on a flat plate model in the Trisonic Wind Tunnel Munich (TWM) for the Mach number range $0.3 \leq Ma \leq 3.0$ and a friction Reynolds number range of $4700 \leq Re_\tau \leq 29\,700$ or $11\,730 \leq Re_{\delta_2} = \rho_e u_e \theta^* / \mu_w \leq 74\,800$. Velocity fields are recorded using planar particle image velocimetry methods (PIV and stereo-PIV) in three perpendicular planes. Using multi-point correlation and spectral analysis methods it was found that the most energetic frequencies have slightly longer streamwise wavelengths for the supersonic case when compared to the subsonic case. Furthermore, a distinct increase in the spanwise spacing of the superstructures was found for the supersonic cases when compared to the subsonic and transonic turbulent boundary layers.

Key words: compressible boundary layers, turbulent boundary layers, boundary layer structure

† Email address for correspondence: matthew.bross@unibw.de

1. Introduction

The coherent structures present in zero pressure gradient (ZPG) turbulent boundary layers have been studied extensively in the past decades and many statistical and structural properties of the flow are well known, as documented in the extensive review by Wallace (2012). Coherent structures are an intrinsic feature of turbulent boundary layers, e.g. the streaky near-wall flow structures visualized by Kline *et al.* (1967) that scale with inner/viscous units or large scale motions (LSM) associated with turbulent bulges that reside in the outer region and are on average only 1–2δ in length (Kovasznay, Kibens & Blackwelder 1970; Balakumar & Adrian 2007). In addition, high- and low-momentum large-scale coherent motions residing in the log-law layer called superstructures have been of particular focus in the last two decades, e.g. Adrian, Meinhart & Tomkins (2000), Ganapathisubramani *et al.* (2005), Hutchins & Marusic (2007*a*), Monty *et al.* (2009), Buchmann *et al.* (2016), de Silva *et al.* (2018). An interesting property of the superstructures is their extension in the streamwise direction, which is on average several boundary layer thicknesses long. These superstructures, much like near-wall streaks, have been shown to meander strongly in the spanwise direction (Hutchins *et al.* 2011). In addition, it has been demonstrated that these structures can carry a relatively large portion of the layer's turbulent kinetic energy, and in effect these superstructures are considered as the main contribution to the formation of a plateau/peak in the streamwise velocity fluctuations in the log-law layer which appears at high Reynolds numbers (Fernholz & Finley 1996; Monty *et al.* 2009; Samie *et al.* 2018). Furthermore, an interaction between superstructures and the near-wall dynamics has been demonstrated (Hutchins & Marusic 2007*b*; Ganapathisubramani *et al.* 2012; Bross, Fuchs & Kähler 2019). Superstructures have also been associated with the low-frequency unsteadiness of the separation bubble downstream of certain shock wave boundary layer interactions (Beresh, Clemens & Dolling 2002; Ganapathisubramani, Clemens & Dolling 2007; Baidya *et al.* 2020), making their impact important for perturbed flows as well. Therefore, the investigation of these superstructures is essential for understanding the overall dynamics of turbulent boundary layers. However, compressibility effects on the coherent structures are by far less studied, mostly due to the many technical challenges these types of flow present.

While compressible wall bounded flows have been intensely studied for many years, the majority of experimental research has focused on the development of scaling models for mean flow properties (Bradshaw 1977; Fernholz & Finley 1980). However, one of the first direct comparisons of compressible and incompressible turbulent boundary layers that included an analysis of the spatial organization of the flow was done by Smits *et al.* (1989) using the correlated signals from a traversed hot-wire for $Ma = 0.1$ and 2.9. They concluded that the spanwise spacing of correlated streamwise features remains unchanged for the subsonic and supersonic cases, but the streamwise length of the correlated mass-flux fluctuations $(\rho u)'$ were twice as big for the subsonic case when compared to the supersonic case. Furthermore, a survey done by Smits & Dussauge (2006) of available supersonic measurements, which mostly used hot-wire probes, concluded that for increasing Mach number and Reynolds number, the streamwise length scales decrease significantly while the spanwise length scales remain unaffected by both Reynolds number and Mach number.

The analysis of the flow structure organization with single hot-wires critically relies on the validity of Taylor's frozen turbulence hypothesis (Taylor 1938), which allows a transformation of a turbulent time signal into the spatial domain if an appropriate convection velocity is selected. In contrast, particle image velocimetry (PIV) can be directly used, without any assumptions, to quantitatively study the spatial organization of velocity fields in a given flow. In the work of Ganapathisubramani, Clemens &

Dolling (2006), elongated streamwise coherent structures in a turbulent boundary layer at $Ma = 2.0$ and $Re_\theta = 35\,000$ ($Re_\tau = 5600$) were visualized by using planar PIV in streamwise-spanwise planes (wall-parallel at $z/\delta = 0.16$ and 0.45), where an underlying similarity to incompressible structures was observed. However, two-point correlations of streamwise velocity fluctuations revealed that the streamwise length scales for the $Ma = 2.0$ turbulent boundary layer were four times larger than incompressible cases reported in the literature, and the spanwise length scale were somewhat larger as well although they were stated to be in good agreement with the subsonic data. The increase in streamwise length scales with Mach number is actually opposite to the conclusion made from the survey of hot-wire measurements in Smits & Dussauge (2006); however they attributed this to a Reynolds number effect or due to the difference between $(\rho u)'$ and u' correlations.

Three-dimensional or volumetric PIV methods are also useful for measuring the anisotropic organization of a flow simultaneously in all directions. However, these approaches often have smaller relative spatial resolution and fields of view when compared to two-dimensional PIV (2-D-PIV) measurements. Nevertheless, Elsinga *et al.* (2010) used tomographic-PIV to investigate structures in a turbulent boundary layer at $Ma = 2.0$ and $Re_\theta = 34\,000$. Using the volumetric data they measured the three-dimensional topology of elongated structures in the log-layer. They showed that the typical width of low-speed regions varied between 0.25δ and 0.4δ and spanwise spacing between 0.5δ and 1δ depending on the wall-normal height.

An important feature of compressible turbulent boundary layers is the variation of thermodynamic flow properties in addition to the velocity across the layer. The effect of compressibility (for Mach numbers below the hypersonic regime) is hypothesized to not influence the turbulent time and length scales (Morkovin 1962), and the thermodynamic properties such as density can be accounted for by their mean variation across the layer. This hypothesis, born out of a semi-empirical approach, has been used extensively in theliterature to compare supersonic mean velocity and fluctuation results to an extensive catalogue of incompressible boundary layer data (Fernholz & Finley 1980; Smits & Dussauge 2006). However, in order to study all the effects of velocity, density, temperature and pressure fluctuations on turbulent structure organization, highly resolved direct numerical simulations (DNS) are required to examine all variables. While DNS of turbulent boundary layers have fine spatial resolution, these simulations often come at a cost of relatively small spatial simulation domains, relatively short simulation times and relatively small Reynolds numbers, which in the case of a turbulent boundary layer limits the amount of scale separation between the inner and outer scales. Nevertheless, an analysis of turbulent flow structures in a $Ma = 2.0$ turbulent boundary layer at $Re_\tau = 1120$ or $Re_{\delta_2} = 3900$ can be found in DNS by Pirozzoli & Bernardini (2011). Therein, it was shown that the streamwise length scales do not change when compared to the incompressible case, while the spanwise velocity length scales are slightly larger for the computed supersonic flow when compared to experimental incompressible data. Interestingly, these results are in contrast to the aforementioned experimental studies, albeit in different ways.

Large-scale coherent motions were also identified in a Mach 3 turbulent boundary layer DNS up to $Re_\theta < 2600$ by Ringuette, Wu & Martín (2008). Alternating high- and low-speed structures were visualized in the log-law layer with an average spanwise structure width of 0.4δ based on $(\rho u)'$ correlations. They also looked at the streamwise extent of low-speed structures at a wall-normal location of $z/\delta = 0.2$ by transforming the simulated time domain into space with Taylor's frozen turbulence hypothesis and

identified low-speed structures up to 100δ in length in instantaneous u-velocity fields. These results were then compared to the incompressible turbulent boundary layer hot-wire measurements of Hutchins & Marusic (2007*a*). It was found that the superstructures for both the incompressible and compressible cases were similar, despite the order of magnitude difference in Reynolds number. While the extent of instantaneous structures could not be truly compared because the effective spatial domain of the hot-wire measurements was around 20δ, Ringuette *et al.* (2008) report that the spanwise spacing of the structures for both cases is approximately 0.5δ.

The structural properties reported in the aforementioned numerical and experimental investigations are not consistent, and a consensus on the reason for the observed differences has not been reached. It is likely however that some of the lack of consensus is due to the fact that past experiments were performed in different facilities having differing boundary and flow conditions (which is also the case for DNS) and measurement techniques, which possibly contributes to the lack of consistency in terms of the characteristics of superstructures. Therefore, the main motivation for the current study is to experimentally investigate the structural topology and statistical properties turbulent superstructures at subsonic, transonic and supersonic Mach numbers in the same test facility by means of state-of-art PIV techniques. The analysis presented herein focuses on the characterization of the streamwise and spanwise length scales of superstructures in the log-law layer over a Mach number range of $0.3 \leq Ma \leq 3.0$.

2. Experimental systems and methods

2.1. *Wind tunnel facility*

The Trisonic Wind Tunnel Munich (TWM) is a blow-down type wind tunnel with a 300 mm $\times$ 675 mm ($w \times h$) test section. A two-throat system consisting of an adjustable Laval nozzle upstream of the test section and an adjustable diffuser downstream of the test section allows for a stable operating Mach number range from 0.3 to 3.0. The stagnation pressure is controlled by a pressure regulation valve and is adjustable between $p_0 = 1.2$ bar and 5.0 bar. This allows the Reynolds number to be set independently of the Mach number. The corresponding Reynolds number (Re_x) range is $(4\text{–}78) \times 10^6$ m^{-1}, which depends on the Mach number. The stagnation pressure p_0 and temperature T_0 are recorded by two sensors in the settling chamber. The facility has two storage tanks that can be pressurized up to 20 bar above ambient pressure, with each tank holding a volume of 178 m^3 of dry air. This amount of air is sufficient for run times in the order of 100 s for the cases discussed below. The wind tunnel's test section is enclosed by a plenum chamber and also has the ability to apply boundary layer suction at both the vertical and the horizontal walls independently. A detailed description of the freestream velocity and pressure fluctuations in the TWM can be found in Scharnowski, Bross & Kähler (2019).

A flat plate boundary layer model was mounted in the test section of the TWM for this investigation. A sketch of the model and coordinate system is shown in figure 1. The overall length of the model in the streamwise direction is 1.70 m, resulting in a turbulent boundary layer thickness of 13–27 mm at a location 1.26 m downstream of the leading edge. A cavity was milled out on the bottom side of the plate where a resistance based temperature sensor was installed in order to estimate the wall temperature T_w. The fluid properties in the freestream are calculated using the isentropic expansion equations and are denoted with the subscript e, e.g. the edge temperature T_e. Since the temperature of the wall is known and the static pressure at the edge is the same at the wall ($p_e = p_w$), ρ_w can be calculated from the ideal gas law. The viscosity at the wall and the edge is estimated

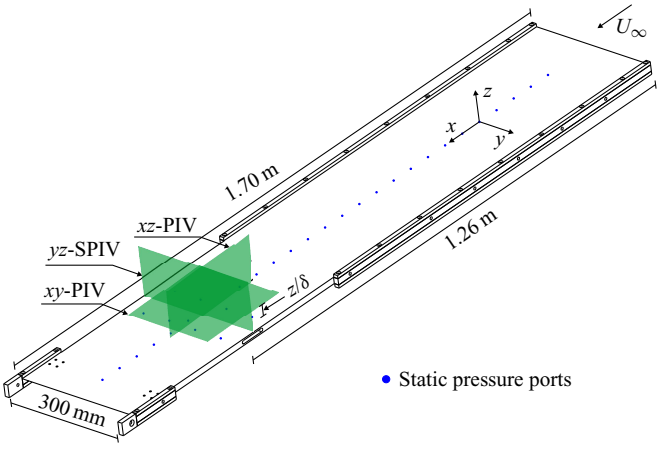

Figure 1. Flat plate boundary layer model used in the Trisonic Wind Tunnel Munich (TWM). Planar PIV measurement planes' locations and orientations are indicated and labelled. The coordinates (x, y, z) correspond to streamwise, spanwise and wall-normal directions respectively.

Ma_e		0.3	0.5	0.8	0.8	2.0	2.0	3.0
p_0	(bar)	1.5	1.5	1.5	3.0	2.2	4.5	4.5
T_0	(K)	288	287	288	287	287	287	288
T_e	(K)	284	277	257	255	160	161	103
ρ_e	$(\mathrm{kg\,m^{-3}})$	1.72	1.60	1.34	2.69	0.61	1.25	0.41
μ_e	$(\mathrm{Ns\,m^{-2}}) \times 10^{-5}$	1.82	1.78	1.68	1.63	1.13	1.09	0.71
ν_e	$(\mathrm{N^2\,s^{-1}}) \times 10^{-5}$	1.06	1.11	1.26	0.61	1.84	0.87	1.80
u_e	$(\mathrm{m\,s^{-1}})$	101	167	256	256	508	508	613
T_w	(K)	288	288	287	285	283	283	282
ρ_w	$(\mathrm{kg\,m^{-3}})$	1.68	1.52	1.18	2.39	0.34	0.71	0.15
μ_w	$(\mathrm{Ns\,m^{-2}}) \times 10^{-5}$	1.81	1.80	1.80	1.79	1.77	1.77	1.79
ν_w	$(\mathrm{N^2\,s^{-1}}) \times 10^{-5}$	1.07	1.19	1.52	0.75	5.35	2.50	12.1
Re_x	$(\mathrm{m^{-1}}) \times 10^6$	9.50	15.5	21.2	42.3	28.4	58.2	35.5

Table 1. Fluid properties at the edge (e) and surface of the flat plate or wall (w).

from the Sutherland Model, which is shown in (2.1) (Sutherland 1883).

$$\frac{\mu_w}{\mu_{ref}} = \frac{T_{ref} + S}{T_w + S} \left(\frac{T_w}{T_{ref}} \right)^{3/2} \tag{2.1}$$

This model is applicable for dry air for a temperature range between 100 K and 1900 K where $S = 110.3$ K (Ames Research Staff 1953). A reference temperature $T_{ref} = 273$ K and viscosity $\mu_{ref} = 1.716 \times 10^{-5}$ $(\mathrm{kg\,ms^{-1}})$ was used. The fluid properties in the settling chamber and the test section are outlined in table 1 for the range of Mach numbers and Reynolds numbers considered in this investigation.

2.2. *Turbulent boundary layer transition*

Transitional devices affixed near the leading edge of aerodynamic surfaces are commonly used to ensure laminar/turbulent transition or to fix the transition location. These types

of devices are often used to thicken the boundary layer, which is often desirable for measurements in high speed flows when the boundary layer thickness is very thin. However, these devices can produce unwanted flow features such as longitudinal vortices or a blockage that can influence coherent flow structures in turbulent incompressible boundary layers and condition the results of a measurement if an inadequate transition or perturbation is selected (Elsinga & Westerweel 2012; Hutchins 2012; Marusic *et al.* 2015; Sanmiguel Vila *et al.* 2017). Furthermore, it was shown (Bross, Scharnowski & Kähler 2018) that even very conservative tripping devices with a height one half the laminar boundary layer thickness can produce a long wake that persists along the surface of the plate for a supersonic turbulent boundary layer, and it must be expected that they influence the near-wall flow features. Therefore, to avoid non-canonical flow perturbations, tripping devices were not applied to the leading edge of the flat plate boundary layer model used in this investigation.

To estimate the location of the natural (un-tripped) transition location for the subsonic and supersonic cases, oil film techniques were applied. A film of an oil mixture, consisting of petroleum oil, linseed oil, oleic acid and TiO_2 particles, was applied to the plate in a homogeneous manner by using a industrial paint sprayer device before each wind tunnel run. The aluminium plate surface was anodized black, which allowed for better contrast with the white TiO_2 particles. The oil film streaks then were captured with two side-by-side sCMOS cameras, creating a field of view spanning the entire test section width. The plate was illuminated with a white LED diffuse light source to create sufficient contrast and homogeneous illumination.

In addition, the flat plate model was designed with a sharp leading edge so that for the supersonic cases the strength of the shock is minimized by forcing an attached shock at the leading edge. For the subsonic case shown in figure 2(*a*) the sharp leading edge produces a small laminar separation which re-attaches approximately 6–7 mm downstream of the leading edge. An elliptically shaped leading edge can be used to avoid flow separation and reduce or eliminate unsteady loading on the plate or move the turbulence transition location downstream. However, for the investigation of a turbulent boundary layer developing over a long flat plate, the separation bubble at the leading edge for subsonic conditions can be considered as a type of transition element where the transition occurs in the shear layer at or near the bubble interface (Hain, Kähler & Radespiel 2009). Therefore, it can be expected that when the flow reattaches, a fully turbulent flow exists that includes a broad spectrum of turbulent scales and does not contain artificially generated coherent flow motions as typically found in the wake of transition devices. For the supersonic case shown in figure 2(*b*), the natural – i.e. unforced – transition location can be estimated by observing the transition wedge pattern near the leading edge. Transition wedges can only be observed where the flow is still laminar. Therefore, the transition location appears to be between 10 and 30 mm downstream of the leading edge for the subsonic and supersonic cases, respectively, which is very far upstream of the measurement location (50–90δ_{99} depending on the Mach number) so that enough boundary layer thickness turn-overs exist for the flow to develop.

2.3. *Side wall and corner effects*

In order to characterize the effect of the side-wall boundary layer development and corner vortices, stereo-PIV (SPIV) measurements were performed in the cross-stream plane (yz-plane) approximately 1.3 m downstream of the leading edge of the flat plate shown in figure 1. The spanwise location of the measurement plane was adjusted such that both

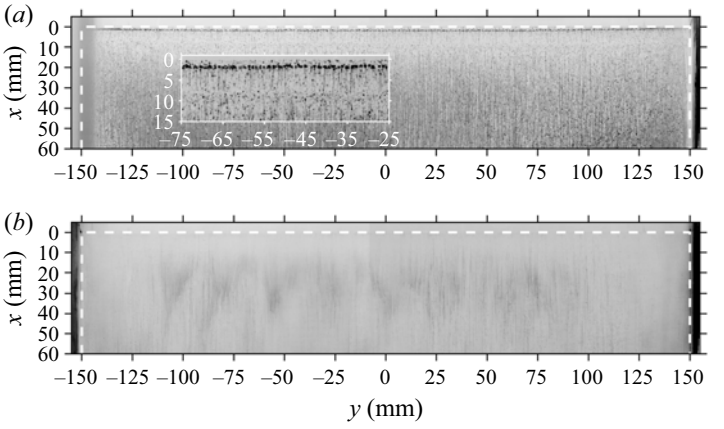

Figure 2. Oil film visualization (*a*) $Ma = 0.3$ and $p_0 = 1.5$ and (*b*) $Ma = 2.0$ and $p_0 = 2.2$ in the leading edge region of the flat plate boundary layer model. The leading edge and spanwise boundaries of the plate are outlined with a white dashed line where $(x, y) = (0\text{ mm}, 0\text{ mm})$ is located at the leading edge and spanwise mid-point of the flat plate. Insert in (*a*) shows an enlarged more detailed view of the leading edge region for the subsonic case.

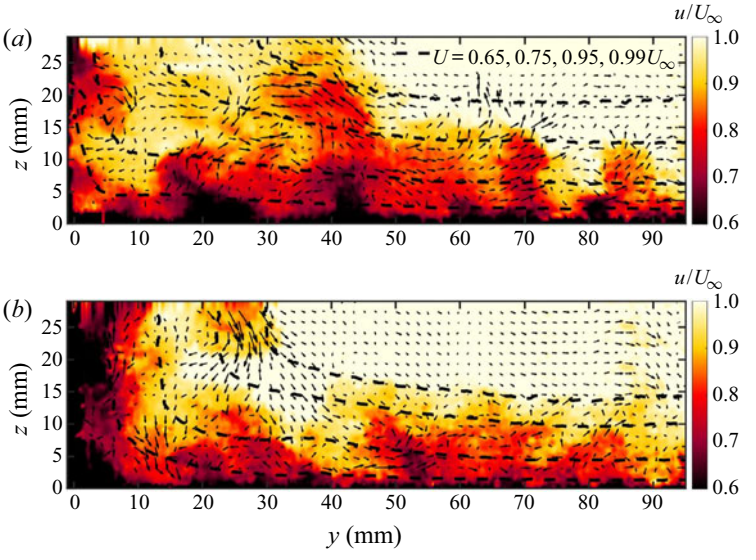

Figure 3. Instantaneous streamwise velocity u field normalized with U_∞ in a spanwise (y) wall-normal (z) SPIV plane for (*a*) $Ma = 0.3$ and $p_0 = 1.5$ and (*b*) for $Ma = 2.0$ and $p_0 = 2.2$. (- -) contour lines correspond to lines of constant mean streamwise velocity U for $U = 0.65$, 0.75, 0.95 and $0.99U_\infty$. In this plane, positive u velocity is directed out of the page and $(y, z) = (0\text{ mm}, 0\text{ mm})$ correspond to the wind tunnel side wall and plate surface locations, respectively.

the side-wall of the wind tunnel and the flow extending approximately 100 mm towards the centre of the tunnel were visible. The results of this measurement for a supersonic and supersonic case are shown in figures 3(*a*) and 3(*b*).

The presence of corner vortices and turbulent structures in the near side-wall and corner regions is evident from the instantaneous velocity fields for both subsonic and supersonic cases shown in figures 3(*a*) and 3(*b*). However, the influence of coherent flow motions

seems to be limited to less than 60 mm from the side-wall. This is confirmed by the fact that contours of constant mean streamwise velocity corresponding to $U = 0.65$, 0.75 and $0.99U_\infty$ appear to converge for all wall-normal heights at spanwise distances greater than 60 mm. As the middle of the flat plate is located at 150 mm from the side wall, it can be concluded that the influences of the side-wall and corner flow are negligible in the centre of the test-section.

2.4. *Quantitative flow field measurements via PIV*

In order to quantitatively characterize the structural topology and spatial velocity statistical properties of the flow, velocity fields using PIV were obtained in three perpendicular planes as shown in figure 1. Planar 2-D-PIV was used in a streamwise wall-normal plane (xz-plane) and wall-parallel planes (xy-plane). In addition, SPIV measurements, different to the SPIV measurement setup shown in § 2.3 and centred at the midspan of the plate, were performed in the cross-stream direction (yz-plane); this provided all three velocity components (u, v, w).

The flow was seeded with Di-Ethyl-Hexyl-Sebacat (DEHS) tracer particles with a mean diameter of around 1 µm, as described by Kähler, Sammler & Kompenhans (2002). The response time of these droplets is approximately 2 µs (Ragni *et al.* 2011). A beam emanating from a Quantel Evergreen 200 Nd:YAG double pulsed laser was formed into a 500 µm thick light sheet in order to illuminate the tracer particles in the aforementioned measurement planes.

The PIV measurements analysed herein were obtained using classical double frame imaging, see Raffel *et al.* (2018) for a detailed description of this measurement technique. Pairs of images are recorded separated by a short time delay Δt, and then sets of these double frame recordings are acquired in a sequence at a frequency of 15 Hz using specially suited sCMOS cameras. Approximately 1000 double frame recordings were acquired for each measurement case and nine different Δt between 0.2 µs and 4 µs were used. The selection of the proper Δt depended on both the optical magnification and the flow speed. In this case, the selected Δt corresponded to a mean particle image shift between $\Delta x \approx 2$ pixels and 10 pixels close the wall and in the freestream, respectively. For all of the measurements, Makro-Planar Zeiss camera objectives were used to ensure excellent imaging quality. The PIV recordings were evaluated using state-of-the-art PIV software including multi-pass image deformation and Gaussian window weighting. The final interrogation window size was varied between 16×16 pixels and 24×24 pixels depending on the measurement plane, see table 2. The selection of the window size essentially fixes the spatial resolution of the measurement – i.e. the smallest possible length scale or structure that can be resolved corresponds to the size of the window as length scales smaller than the window size will be spatially low-pass filtered. However, since large-scale structures are the focus of this investigation, the spatial resolution of the presented measurements is sufficient; more details can be found in § 4. A 50 % window overlap was used, which made the final vector spacing half of the window size used for the particle image correlation.

For each of the planes measured, a different camera and light sheet orientation was used. The streamwise wall-normal plane (xz-direction) was imaged by two sCMOS cameras which were mounted side by side in the x-direction such that they had overlapping fields of view (FOV) that observed the laser sheet perpendicularly. The recorded camera images were then stitched together resulting in a final field of view of 500 mm × 50 mm (in x and z, respectively) and scaling factor of 37.0 µm pixels^{-1}. For this plane, the

Parameter			*xz*-PIV	*xy*-PIV	*yz*-SPIV
Recording rate	f	(Hz)	15	15	15
Scaling factor	m	(μm px^{-1})	37.0	67.5	26.1
Magnification	M		0.18	0.10	0.42
Field of view	FOV	(mm^2)	175 × 40	176 × 149	81 × 45
Final window size	IW	(px^2)	16 × 16	16 × 16	24 × 24
		(mm^2)	0.59 × 0.59	1.1 × 1.1	0.48 × 0.48
Number of vectors			594 × 135	320 × 270	340 × 187

Table 2. Imaging parameters for particle image velocimetry (PIV) measurements.

magnification, calculated by dividing the pixel pitch of the camera (6.5 μm px^{-1}) by the scaling factor, was $M = 0.18$. The wall-parallel plane (xy-direction) was imaged using one sCMOS camera that was mounted on top of the wind tunnel to view a wall-parallel aligned light sheet perpendicularly. In order to observe a relatively large FOV in the streamwise and spanwise directions, a short focal length camera objective was used, which resulted in a FOV of 180 mm × 140 mm (in x and y, respectively) with a scaling factor of 67.5 μm pixels^{-1} and magnification of $M = 0.10$. Finally, a higher resolution measurement was done in the cross-stream plane (yz-direction) where SPIV was used to measure all three perpendicular velocity components. The SPIV setup consisted of two sCMOS cameras mounted on the same side of the wind tunnel but aligned on either side of the cross-stream oriented light sheet. In this case the resulting FOV was 70 mm × 45 mm (in y and z, respectively) with a scaling factor of 26.1 μm pixels^{-1} and a magnification of $M = 0.42$. For the SPIV plane, all the Mach and Reynolds numbers listed in table 1 were measured, while for the wall-parallel plane, only $Ma = 0.3$ $p_0 = 1.5$, $Ma = 0.8$ $p_0 = 1.5$, $Ma = 2.0$ $p_0 = 2.2$ and $Ma = 3.0$ $p_0 = 4.5$, and were considered. Finally, for the streamwise wall-normal plane, only $Ma = 0.3$ $p_0 = 1.5$ and $Ma = 2.0$ $p_0 = 2.2$ were considered.

3. Mean flow field

In order to compare compressible and incompressible flows, the velocity fields measured with PIV must be corrected/scaled so that the mean variation of temperature and density across the boundary layer are taken into account. Therefore, it is essential for the structural analysis that the mean velocity field is properly scaled. In this section, the methods for scaling compressible flows so that they can be compared to incompressible results are outlined. The governing scaling equations for the mean flow in turbulent incompressible turbulent boundary layers often involve a classification of different regions of the layer, such as a linear near-wall region, a logarithmic layer or the wake region, e.g. Coles (1956). However, classical incompressible velocity scaling is not applicable for compressible cases where the thermodynamic properties of the flow change across the layer because the mean streamwise velocity scaled with inner units ($\bar{u}^+ = \bar{u}/u_\tau$) diverges from the log-law with increasing Mach number. In order to more adequately compare compressible and incompressible experimental or numerical results, an extension of the scaling laws to the compressible regime can be made using the Van Driest effective velocity given by the following differential equation: $\mathrm{d}u_{vd} = (\bar{\rho}/\rho_w)^{1/2}\,\mathrm{d}\bar{u}$ (Van Driest 1951). Using a semi-empirical approach, the Van Driest velocity can be written in the form

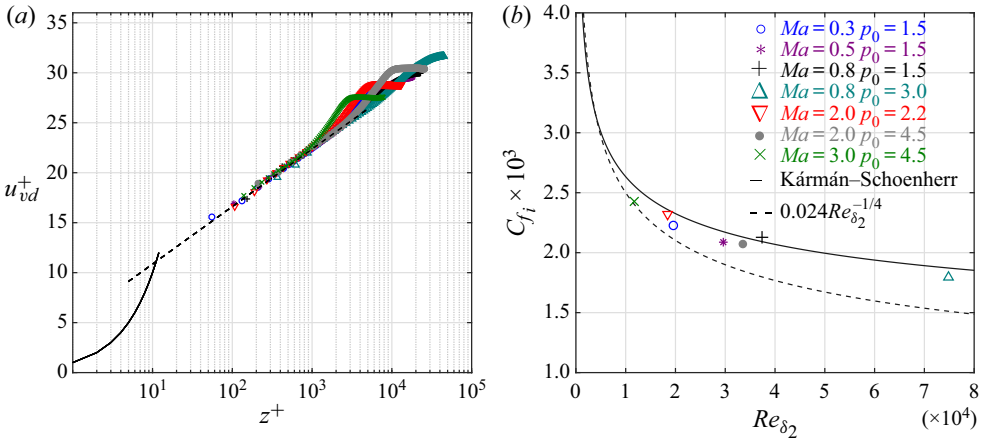

Figure 4. (*a*) Van Driest transformed, u_{vd}^+, mean profiles vs. inner scaled wall-normal distance z^+ for $0.3 \leq Ma \leq 3.0$ evaluated from the cross-stream SPIV measurement. Also shown is the $u^+ = z^+$ indicated by the solid line and the dashed line represents $u^+ = \log(z^+)/0.41 + 5.6$. (*b*) Skin friction $C_{fi} = F_c C_f$ estimate transformed with *Van Driest II* vs. transformed momentum thickness Reynolds number Re_{δ_2}.

shown in (3.1).

$$u_{vd} = \frac{u_e}{B} \sin^{-1}\left(\frac{2B^2(\bar{u}/u_e) - A}{\sqrt{A^2 + 4B^2}}\right), \tag{3.1}$$

where the constants A and B are as follows:

$$A = \left(1 + r\frac{\gamma - 1}{2} Ma_e^2\right)\frac{T_e}{T_w} - 1, \quad B^2 = r\frac{\gamma - 1}{2} Ma_e^2 \frac{T_e}{T_w}, \tag{3.2a,b}$$

$r \approx 0.9$ (recovery factor typical for turbulent boundary layers) and the specific heat ratio is $\gamma = 1.4$ for air in the temperature and pressure ranges occurring for the flow cases considered herein. Using inner scaling, the compressible version of the log-law layer can be expressed in a similar way as the incompressible log-law layer as shown in (3.3) (Bradshaw 1977; Fernholz & Finley 1980; Smits & Dussauge 2006).

$$u_{vd}^+ = \frac{u_{vd}}{u_\tau} = \frac{1}{\kappa}\log\left(\frac{u_\tau z}{\nu_w}\right) + C^* + \frac{2\Pi}{\kappa}\sin^2\left(\frac{\pi}{2}\frac{z}{\delta_c}\right). \tag{3.3}$$

The mean streamwise velocity profile shown in figure 4(*a*) was computed by transforming $\bar{u}$ with (3.1) for the range of Mach and Reynolds numbers investigated. For these profiles the mean velocity data was taken from the centre-line of the yz-plane in the SPIV measurement. The wall position was determined by visual inspection of the wall location from the PIV images, and then the profiles were systematically shifted in sub-pixel increments in order to obtain a good least-squares fit to (3.3). The mean flow parameters calculated from this fitting procedure are provided in table 3. The resulting Van Driest transformed mean streamwise velocity profiles in figure 4(*a*) demonstrate a nice collapse in the log-law layer for all the Mach numbers investigated.

The friction velocity determined from aforementioned fitting procedure can be used to estimate the skin friction coefficient using the relation $C_f = (2u_\tau^2 \rho_w)/(\rho_e u_e^2)$. However, in order to compare the skin friction coefficient for sub- and supersonic flows, a transformation of the form $C_{fi} = F_c C_f$ is necessary. A variety of transformation functions

Ma_e		0.3	0.5	0.8	0.8	2.0	2.0	3.0
p_0	(bar)	1.5	1.5	1.5	3.0	2.2	4.5	4.5
δ_{99}	(mm)	24.5	25.8	27.0	27.7	14.0	13.2	14.0
θ^*	(mm)	2.1	2.1	2.0	2.0	1.1	0.96	0.87
δ^*	(mm)	2.7	2.8	3.2	3.2	5.3	5.3	8.8
u_τ	($\mathrm{m\,s^{-1}}$)	3.43	5.55	8.49	8.04	18.2	17.2	23.8
$C_f \times 10^3$	(−)	2.22	2.11	1.93	1.75	1.47	1.30	1.09
$C_{f_i} \times 10^3$	(−)	2.23	2.09	2.13	1.79	2.32	2.07	2.43
Re_τ	(−)	7800	12 030	15 210	29 720	4680	9150	2760
Re_θ	(−)	19 370	30 110	40 030	81 180	29 120	54 370	28 380
Re_{δ_2}	(−)	19 570	29 610	37 400	74 850	18 420	33 540	11 730

Table 3. Mean boundary layer parameters. Friction based Reynolds number Re_τ is evaluated at the wall. The skin friction coefficient $C_f = (2u_\tau^2\rho_w)/(\rho_e u_e^2)$ is transformed to $C_{f_i} = F_c C_f$, where F_c is given in (3.4).

(F_c) exist, but the so-called *Van Driest II* (Van Driest 1956) version, which has been shown to fit well to experimental data over a large range of Reynolds numbers (Hopkins & Inouye 1971; Bradshaw 1977), is widely used. Therefore, we implement the *Van Driest II* formulation found in Hopkins & Inouye (1971), $C_{f_i} = F_c C_f$ where,

$$F_c = \frac{\Psi}{(\arcsin\alpha + \arcsin\beta)^2}, \tag{3.4}$$

where $\Psi = ((\gamma - 1)/2) r M_e^2 = 0.2 r M_e^2$ and,

$$\left.\begin{aligned} \alpha &= \frac{\left(2A^2 - B\right)}{\left(4A^2 + B^2\right)^{1/2}} \quad \text{and} \quad \beta = \frac{B}{\left(4A^2 + B^2\right)^{1/2}}, \\ A &= \left(\frac{\Psi}{T_w/T_e}\right)^{1/2} \quad \text{and} \quad B = \frac{(1 + \Psi - T_w/T_e)}{T_w/T_e}. \end{aligned}\right\} \tag{3.5}$$

The *Van Driest II* transformed skin friction coefficients C_{f_i} for all the measured cases are plotted as a function of transformed momentum thickness Reynolds number Re_{δ_2} (see (3.8*c*)) in figure 4(*b*). The solid and dashed lines plotted in figure 4(*b*) are two widely used semi-empirical skin friction coefficient correlations, namely the Kármán–Schoenherr (Schoenherr 1932; von Kármán 1934; Hopkins & Inouye 1971) and a power-law based fit $C_{f_i} = 0.024 Re_{\delta_2}^{-1/4}$ from Smits, Matheson & Joubert (1983). In general, the transformed C_{f_i} follows the semi-theoretical skin friction correlations; however for increasing Reynolds number, the C_{f_i} values lie closer to the Kármán–Schoenherr correlation, which is in agreement with the findings of Hopkins & Inouye (1971) for high Reynolds number data. The $0.024 Re_{\delta_2}^{-1/4}$ fit is perhaps more suitable for low-Reynolds number data as it was deduced from data at $Re_\theta < 3000$ in Smits *et al.* (1983). It must be stated that the C_{f_i} values reported here are the result of an indirect method that fits the log-law layer to determine u_τ values for each case. However, despite the many assumptions and possible fitting errors contained in this indirect method, the results shown in figure 4(*b*) provide some validation that the C_{f_i} estimation is in reasonable agreement with well established semi-empirical relations, and therefore determining the skin friction with this indirect method is at least sufficient for scaling purposes.

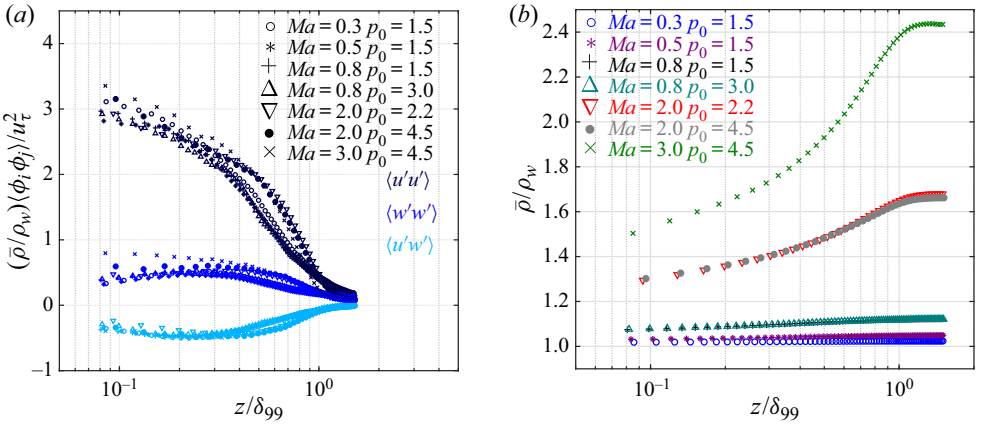

Figure 5. (*a*) Morkovin scaled Reynolds stress profiles vs. outer scaled wall-normal distance (z/δ_{99}) for $0.3 \leq Ma \leq 3.0$ computed from the cross-stream SPIV measurement. (*b*) Mean flow density $\bar{\rho}$ normalized with fluid density at the wall ρ_w. The mean flow density $\bar{\rho}$ in z-direction is calculated from the Walz transformation of the mean streamwise velocity profile $\bar{u}$.

In addition to the mean flow, the scaling of fluctuations in compressible turbulence must be also carefully considered. In compressible turbulent flows,velocity, temperature and pressure/density all fluctuate, which can be characterized as vorticity, entropy and acoustic variations, respectively (Kovasznay 1953). As long as the Mach number is not too large, i.e. the local effects of compressibility are small, the acoustic/pressure and entropy/temperature fluctuations can be considered negligible. Using this idea, Morkovin hypothesized that for sub-hypersonic Mach numbers the compressibility effects on the adiabatic turbulent boundary layer dynamics are small, and therefore the boundary layer structure should be the similar to the incompressible case (Morkovin 1962). Furthermore, Morkovin's hypothesis infers that the turbulent length and time scales are not influenced by compressibility and the shear and normal stress distributions can be scaled with $\bar{\rho}/(\rho_w u_\tau^2)$, which is otherwise known as Morkovin scaling (Bradshaw 1977; Smits & Dussauge 2006).

The Morkovin scaled Reynolds stress profiles for the range of Mach and Reynolds numbers are provided in figure 5(*a*). In general, there is a good collapse of the profiles across all Mach numbers and Reynolds numbers, which supports Morkovin's hypothesis. For the region $z/\delta_{99} > 0.5$ all stress components are slightly elevated for the supersonic cases when compared to the subsonic Mach numbers. However, for the majority of the log-law region the Morkovin scaled profiles are in relatively good agreement, indicating that the mean values of streamwise turbulent fluctuations in the regions where superstructures reside are comparable for all the measurement test cases.

However, when compared to a variety of profiles available in the aforementioned literature review, the magnitude of the wall-normal stress component in figure 5(*a*) is lower than previously reported. In these studies, the Morkovin scaled turbulent fluctuation r.m.s. or intensity approaches 1 in the log-law layer while the wall-normal Morkovin scaled r.m.s. fluctuations trend towards $(\sqrt{\bar{\rho}/\rho_w}/u_\tau)\sqrt{\langle w'^2\rangle} \approx 0.8$ for the current data set. The attenuation of the mean fluctuations could be associated with the spatial filter of the SPIV measurement technique used for this study. This method is perhaps not the most suitable for obtaining higher order statistics or resolving small fluctuations due to the technique's higher sensitivity to vibrations and optical aberrations (Sciacchitano 2019). However, the bias in the fluctuation intensity magnitude seems to be rather consistent across the

measured cases, and since the post-processing methods for all cases were identical, the profiles presented in figure 5(*a*) can be considered as a fair comparison across all the cases. Furthermore, the purpose of the measurements was to characterize the average spatial distribution of δ scaled structures and it is not expected that any bias in the turbulent intensity fluctuation magnitude influences the spatial structure patterns in the following sections. This is further supported by the good agreement between the spanwise structure spacing calculated in §§ 4.2 and 4.3 from SPIV and standard planar-PIV measurements.

The Reynolds stress results presented herein support the validity of Morkovin scaling for the comparison of supersonic and subsonic data, particularly in the log-law layer. However, this scaling is only generally valid for $Ma < 5$ or when the fluctuating Mach number is below 0.3 (Smits & Dussauge 2006). This scaling does not necessary hold for all regions in the boundary layer, as pointed out in a recent DNS study of a Mach 2 turbulent boundary layer (Wenzel *et al.* 2018) where the validity of the Van Driest and Morkovin scaling was systematically investigated. They demonstrated that both the Van Driest and Morkovin scaled profiles are slightly influenced by Mach number in the near-wall and wake regions.

In order to use the Morkovin scaling in the analysis in § 4, the mean density profile across the boundary layer must be known. To obtain the density profile the Walz transformation (Walz 1966) shown in (3.6) was used to calculate the temperature profile based on the mean streamwise velocity profile.

$$\frac{T}{T_e} = \frac{T_w}{T_e} + \frac{T_r - T_w}{T_e}\left(\frac{\bar{u}}{u_e}\right) - r\frac{(\gamma-1)}{2}Ma_e^2\left(\frac{\bar{u}}{u_e}\right)^2. \tag{3.6}$$

The recovery temperature T_r (an adiabatic wall would mean $T_r = T_w$) is defined as

$$T_r = T_e\left(1 + r\frac{(\gamma-1)}{2}Ma_e^2\right). \tag{3.7}$$

The mean temperature profile was then used to calculate the mean density profile using the ideal gas law. The mean density profile normalized with the wall density for different Mach numbers is shown in the figure 5(*b*). For $Ma = 0.3$ there seems to be no change in the density across the boundary layer;however for $Ma = 0.8$ a small variation in the mean density profile across the layer is already visible and for $Ma = 2.0$ and 3.0 the variation is much stronger.

For incompressible turbulent boundary layers, the friction based Reynolds number Re_τ can be viewed as the ratio of large scales (δ) to the small viscous or inner scales. However, for compressible turbulent boundary layers Re_τ is localized and depends on the wall-normal location. Notably, Re_τ at the wall becomes small for $Ma = 2.0$ and 3.0 despite having large u_τ due to the increasing kinematic viscosity at the wall. Therefore, the Re_τ reported in table 3 was only evaluated at the wall. A more suitable Reynolds number often used for compressible turbulent boundary layers is based on the momentum thickness is $Re_{\delta_2} = \rho_e u_e \theta^*/\mu_w$ where momentum thickness θ^* is shown in (3.8*a–c*) and (3.9*a*,*b*). The displacement thickness δ^* is also given in (3.9*a*,*b*). The incompressible friction based Reynolds numbers Re_τ and Re_θ, and the compressible Re_{δ_2} shown in (3.8*a–c*) are summarized in table 3 for all Mach numbers. As expected for the subsonic Mach numbers particularly for $Ma = 0.3$ and 0.5 there is not much difference between Re_θ and Re_{δ_2}. However, starting with $Ma = 0.8$ the difference between these values is visible and

becomes more dramatic with increasing Mach number.

$$Re_\tau = u_\tau \delta_{99}/\nu_w; \quad Re_\theta = u_\infty \theta^*/\nu_e; \quad Re_{\delta_2} = \rho_e u_\infty \theta^*/\mu_w, \tag{3.8a–c}$$

$$\theta^* = \int_0^{\delta_{99}} \frac{\bar{\rho}}{\rho_e}\frac{\bar{u}}{u_\infty}\left(1 - \frac{\bar{u}}{u_\infty}\right) \mathrm{d}z; \quad \delta^* = \int_0^{\delta_{99}} \left(1 - \frac{\bar{\rho}}{\rho_e}\frac{\bar{u}}{u_\infty}\right) \mathrm{d}z. \tag{3.9a,b}$$

The analysis in this section provides the framework for the scaling of compressible (sub-hypersonic) turbulent boundary layers measured herein using the classical approaches found in the literature. The proper scaling of the velocity fields measured with PIV is essential so that the sub- and supersonic cases can be compared with each other in the statistical analysis of structures in the following section.

4. Structural analysis

In the following section the structural properties of the turbulent boundary layers are analysed using multi-point correlations and spatial spectral methods in each of the three perpendicular measurement planes with the aim of characterizing the large-scale superstructures in the streamwise, spanwise and wall-normal directions over the range of Mach numbers investigated herein.

4.1. *Streamwise-wall normal structures*

The organization of the turbulent boundary layer in the streamwise-wall-normal (xz) plane is considered first in this section as this is a commonly presented and discussed plane found in turbulent boundary layer literature. Figures 6(a) and 6(b) shows exemplary instantaneous velocity fields at $Ma = 0.3$, $p_0 = 1.5$ and $Ma = 2.0$, $p_0 = 2.2$ to illustrate typical structural features of the flow such as uniform momentum zones (UMZs). The streamwise extent of the measurement plane was produced by stitching two cameras aligned side by side with a small overlap in the streamwise field of view. The PIV images from each camera are evaluated separately and then the resulting velocity fields are stitched together in the overlap region.

A simple way of detecting features in the turbulent boundary layer is to look for regions of uniform momentum or so-called uniform momentum zones (UMZs). Detailed investigations about the presence of these regions or zones inside incompressible turbulent boundary layers can be found in Meinhart & Adrian (1995) and Adrian *et al.* (2000). More recently, de Silva, Hutchins & Marusic (2016) identified the presence of three to five UMZs using planar double-frame PIV measurements over a few orders of magnitude variation of high Reynolds numbers. These UMZs have also been described in the context of coherent structures as shown in Laskari *et al.* (2018) where the temporal coherence of UMZs using time-resolved PIV of an incompressible ZPG turbulent boundary layer was explored. Within that study, the number of UMZs was related to the presence of a low- or high-momentum large-scale structure moving through the measurement plane. Therefore, the detection of UMZs can be used to interpret the instantaneous structure organization within a turbulent boundary layer.

As most of the previous studies have only considered incompressible flows, a brief demonstration of this detection technique applied to both the subsonic and supersonic measurements is provided. In figures 6(a) and 6(b) instantaneous colour contours of the velocity field u/U_f in the xz-plane are plotted for the $Ma = 0.3$, $p_0 = 1.5$ and $Ma = 2.0$, $p_0 = 2.2$ cases. Overlaid on the colour contours are solid grey contour lines of constant u/U_f that represent the edges or borders of the UMZs for these specific instantaneous

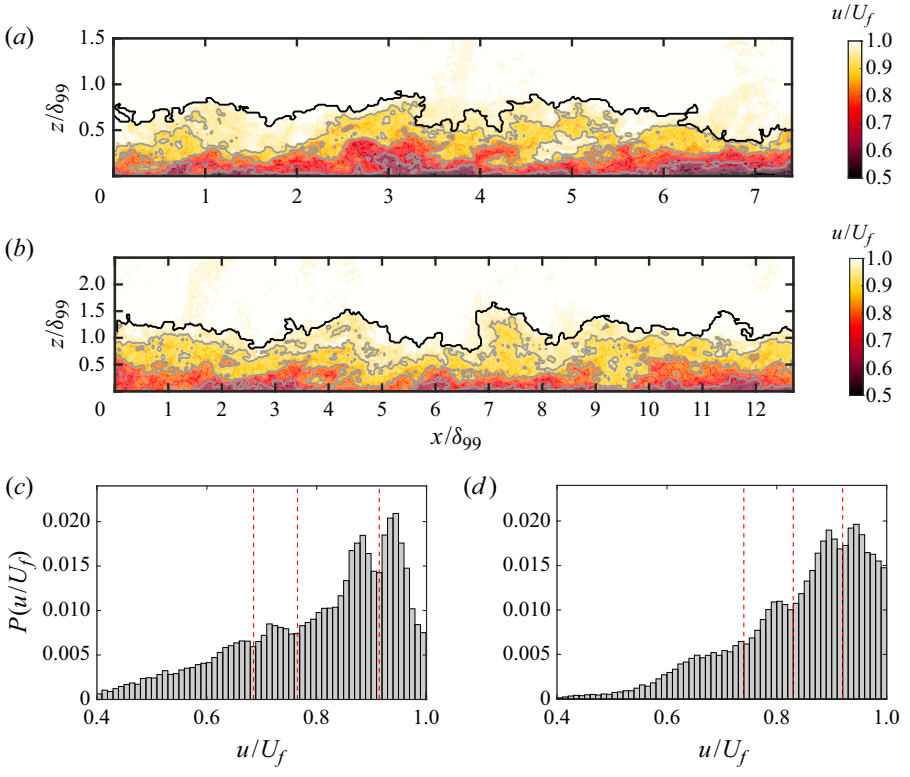

Figure 6. Instantaneous velocity field u/U_f in the xz-plane where $U_f = 0.99U_\infty$ at (*a*) $Ma = 0.3$, $p_0 = 1.5$ and (*b*) $Ma = 2.0$, $p_0 = 2.2$. Wall-normal, z, and streamwise, x, directions are scaled with δ_{99} which is 24.5 and 14 mm for $Ma = 0.3$, $p_0 = 1.5$ and $Ma = 2.0$, $p_0 = 2.2$ respectively. Solid black lines represent the turbulent–non-turbulent interface (TNTI) and solid grey contours lines of constant u/U_f represent the borders or edges the uniform momentum zones (UMZs) determined from the relative probability function (p.d.f.) of the instantaneous velocity field u/U_f for $Ma = 0.3$ and $Ma = 2.0$ in (*c*,*d*) respectively. The borders or edges of the UMZs, indicated with red-dashed lines, are located at the minima between the peaks present in the p.d.f. of u/U_f. Only the turbulent flow region, designated by the TNTI, was considered in the p.d.f. calculation.

velocity fields. In addition, the black solid line overlaid on these velocity fields represents the instantaneous turbulent–non-turbulent interface (TNTI), which was detected using the homogeneity criterion developed by Reuther & Kähler (2018).

The borders or edges of the UMZs are determined from the location of minima between the peaks in the relative probability function (p.d.f.) of u/U_f shown in figures 6(*c*) and 6(*d*). The minima locations are indicated by the vertical red dashed lines and correspond to the values of constant u/U_f used to draw the solid grey contour lines in figures 6(*a*) and 6(*b*). It should be noted that in order to avoid a large peak in the p.d.f. of u/U_f near the boundary layer edge, an exclusion of any non-turbulent parts of the flow designated by the TNTI must be carried out before calculating the p.d.f. for each instantaneous flow field. Therefore, it follows that the TNTI forms the outermost edge or border of the UMZs in the turbulent boundary layer.

In the exemplary instantaneous fields shown in figures 6(*a*) and 6(*b*), four UMZs were detected for both the subsonic and supersonic cases. While an in-depth statistical analysis of the average number of UMZs was not performed, a survey of the instantaneous velocity fields showed a typical number of UMZs between two and four for both the

sub- and supersonic cases, which is consistent with the number reported in the literature for incompressible turbulent boundary layers. In fact a recent study at hypersonic flow conditions detected two to three UMZs in the log-law layer and wake region at $Ma = 7.5$ (Williams *et al.* 2018). Therefore, it can be concluded that the organization of large-scale structures associated with UMZs in the outer flow region remains relatively unchanged for increasing Mach number.

It should be noted that the careful detection of the UMZ edges can depend on the spatial resolution (de Silva *et al.* 2017) of the measurement, particularly in the wall normal direction. Due to the resolution limitations in all the aforementioned literature, including the results analysed herein, the region below $z/\delta < 0.1$ was not well resolved. However, it follows from the known coherent structures in the near-wall region, such as meandering streaks, and their dynamics that UMZs must also exist close to the wall. The presence of near-wall UMZs associated with the viscous sublayer and near-wall streaks was demonstrated in Bross *et al.* (2019) in high spatial and temporal resolved near-wall particle tracking measurements of an incompressible turbulent boundary layer. Therefore, the detection of more UMZs in the compressible data discussed herein would be expected if the spatial resolution in the wall-normal direction was higher. However, as the focus of the present study is on the characteristics of large-scale structures in the outer flow region, the spatial resolution of the present measurements is sufficient.

To determine the mean streamwise elongation of the large-scale coherent flow motions from the correlation of streamwise velocity fluctuations, u', a two point spatial correlation analysis was performed. Plotted in figures 7(*a*) and 7(*b*) are contours of the correlation coefficient R_{uu} at a wall-normal origin location $z_0/\delta_{99} = 0.2$, where $\xi_x = x_o + \Delta x$ with x_0 corresponding to the centre of the FOV in the streamwise direction. Overlaid on the colour contours is a straight line through the centre of the correlations with an inclination angle of 14°. For both the sub- and supersonic cases, the correlation at $z_0/\delta_{99} = 0.2$ appears to have a typical inclination angle of approximately 14°. This is consistent with the inclination angle of the large-scale motions which is widely reported for incompressible ZPG flows, between 12° and 16° (Adrian *et al.* 2000; Marusic & Heuer 2007; Baars, Hutchins & Marusic 2017).

Investigations in compressible flows vary in their results. Rayleigh scattering visualization of density fluctuations from Smith & Smits (1995) estimate between 30° and 60° inclination angle at $Ma = 2.5$. Similarly, multi-probe cross-correlation of hot-wire signals in a $Ma = 3.0$ turbulent boundary layer report inclinations angles of $(u\rho)'$ based structures in the same range as Smith & Smits (1995). In contrast, correlations of u' from PIV measurements of at $Ma = 0.8$ turbulent boundary layers report inclination angles of 12° and 13° (Buchmann *et al.* 2014) and DNS at $Ma = 3.0$ of 17° and 20° (Ringuette *et al.* 2008). Pirozzoli & Bernardini (2011) also report a typical structure angle based on u' of around 14° in their DNS at $Ma = 2.0$. However, Pirozzoli & Bernardini (2011) also report that the structure angles based on density and temperature fluctuations are typically two times larger than the u' structures. This explains why the inclination angles measured with Rayleigh scattering (Smith & Smits 1995) and hot-wires (Spina, Donovan & Smits 1991) in compressible flows are much larger than the velocity based angle calculation.

Considering the streamwise extent of R_{uu}, the correlation appears to be slightly longer (∼20 % increase) for the supersonic case in comparison to $Ma = 0.3$. However, due to low-level correlation below 0.2 with the surrounding field for $Ma = 0.3$, conclusions about the spatial extent of these low correlation values must be made with caution. This low-level correlation could be related to the fact that the nominal freestream turbulence intensity level in this particular blow-down wind tunnel is larger at $Ma = 0.3$ than at $Ma = 2.0$

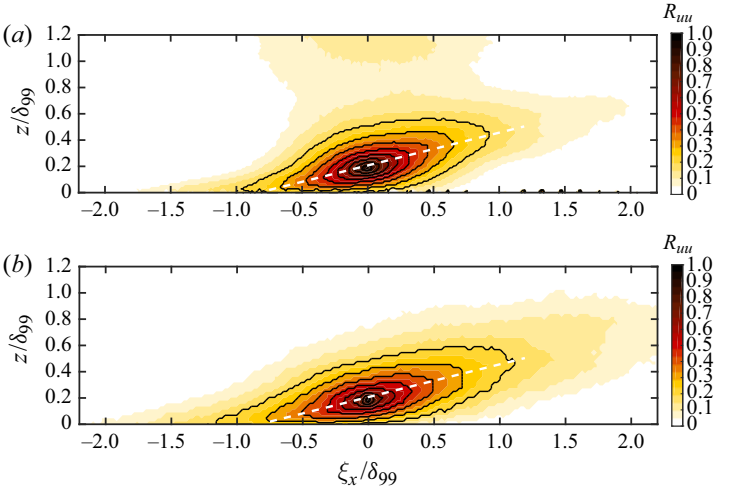

Figure 7. Two-point correlation coefficient R_{uu}, calculated at the wall-normal origin location $z_0/\delta_{99} = 0.2$ for (*a*) $Ma = 0.3$, $p_0 = 1.5$ and (*b*) $Ma = 2.0$, $p_0 = 2.2$. Horizontal axis is $\xi_x = x_0 + \Delta x$ where x_0 is the centre of the field of view. Solid black contour lines range from 0.2 to 1 in 0.1 increments. White dashed line is plotted with 14° inclination angle.

(Scharnowski *et al.* 2019). Nevertheless, the contour lines corresponding to $R_{uu} = 0.2$ undoubtedly appear slightly larger in the streamwise direction.

To examine the dominant frequencies associated with the coherent flow motions, the spectrogram of pre-multiplied power spectral density (PSD) was calculated for $Ma = 0.3$ and 2.0 and is plotted in figures 8(*a*) and 8(*b*). While the velocity fields measured with PIV in this case are only acquired at 15 Hz, the relatively large field of view allows for the spectral content in a spatial sense to be calculated without the assumption of Taylor's hypothesis of frozen turbulence. The *PSD* was computed from vector fields based on an interrogation window size of IW = 16 × 16 pixels with 50 % overlap using the method of Welch (1967). The *PSD* was calculated at each wall normal position using a single Hamming window corresponding to FOV length in the streamwise distance for 1000 statistically independent velocity fields. The spectra for each time step were then averaged together to produce the final *PSD* spectrograms.

The highest resolvable frequency is limited by the vector spacing of the velocity fields and effectively sets the spatial resolution of the measurement. Therefore, the wavelength of the largest resolvable frequency corresponds to the distance between two interrogation windows. With an IW of size 16 px × 16 px the minimum resolvable wavelength corresponds to $\lambda = 0.6$ mm. Likewise, the maximum resolvable wavelength corresponds to the FOV size. However, the *PSD* is actually over sampled due to overlapping interrogation windows, which then corresponds to minimum resolvable wavelengths of 0.3 mm. However, it is important to note that the *PSD* for spatial frequencies higher than (2/IW) does not satisfy the Nyquist criterion and are within the noise floor. Thus, the resolved wavelength range is from 0.6 mm to 175 mm in the streamwise direction, which is sufficient to resolve the features of the large-scale structures.

In these plots the largest values of normalized pre-multiplied velocity spectra, $(\bar{\rho}/\rho_w)k_x\Phi_{uu}/u_\tau^2$, appear in a concentrated region with a maximum at a streamwise wavelength of $\lambda_x/\delta_{99} \approx 4.1$ and 5 for Mach 0.3 and 2.0, respectively, which corresponds to about a 20 % increase. While measurements closer to the wall were not possible in

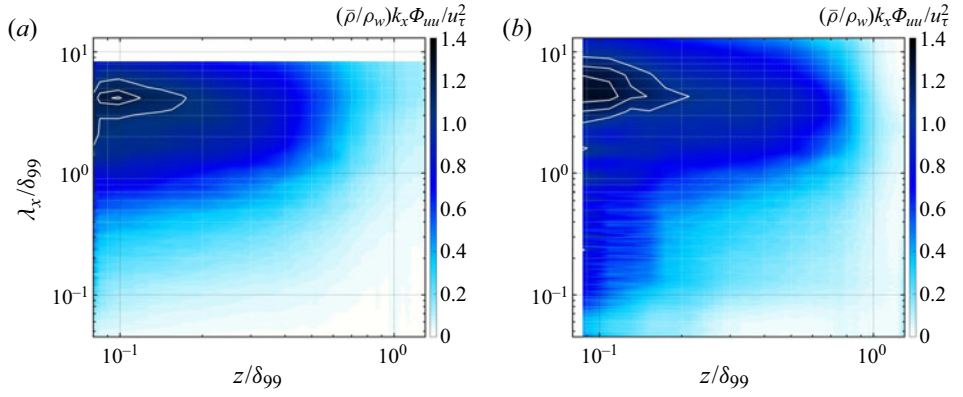

Figure 8. Pre-multiplied streamwise velocity spectrogram $(\bar{\rho}/\rho_w)k_x\Phi_{uu}/u_\tau^2$ for (*a*) $Ma = 0.3$, $p_0 = 1.5$ and (*b*) $Ma = 2.0$, $p_0 = 2.2$ as a function of streamwise wave length, λ_x and wall-normal direction, z scaled with δ_{99}. Solid contour lines correspond to $(\bar{\rho}/\rho_w)k_x\Phi_{uu}/u_\tau^2 = 1.1$, 1.2 and 1.3. The vertical and horizontal axis limits are the same in (*a*) as in (*b*).

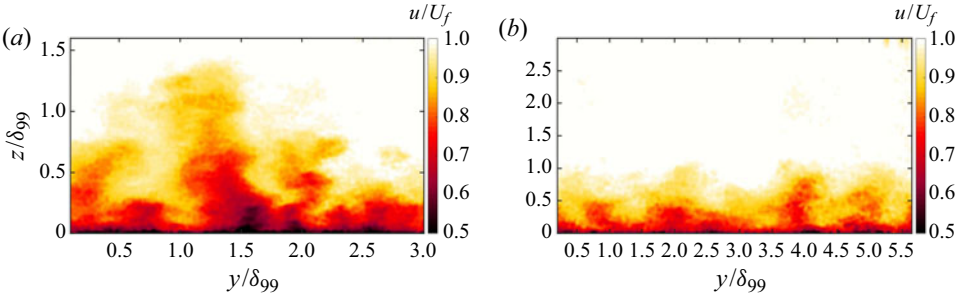

Figure 9. Instantaneous velocity field u/U_f in the yz-plane or SPIV plane, where $U_f = 0.99U_\infty$ at (*a*) $Ma = 0.3$, $p_0 = 1.5$ and (*b*) $Ma = 2.0$, $p_0 = 2.2$. Wall-normal, z, and spanwise, y, directions are scaled with δ_{99}, which is 24.5 and 14 mm for $Ma = 0.3$, $p_0 = 1.5$ and $Ma = 2.0$, $p_0 = 2.2$, respectively.

these experiments, this peak in the spatial spectral plots is indicative of the secondary peak (Fernholz & Finley 1996; Monty *et al.* 2009; Samie *et al.* 2018) in the streamwise velocity fluctuations. Since this peak is associated with the meandering superstructures in the log-law layer, it can be concluded that the superstructures are associated with slightly longer (by approximately ∼20 %) streamwise energetic wavelengths for $Ma = 2.0$ as compared to $Ma = 0.3$.

4.2. *Cross-flow structures*

In order to visualize and analyse the organization of coherent flow structures in the spanwise direction at different wall normal heights, SPIV measurements were performed in a cross-stream plane for all Mach numbers listed in table 1. Exemplary instantaneous velocity fields are shown in figures 9(*a*) and 9(*b*) to illustrate the slope and spanwise spacing of the large-scale structures. In the following, the characteristic spatial distribution of coherent structures in the spanwise direction via multi-point statistics and spatial spectral calculations are presented.

To quantify the average spacing of superstructures in the spanwise direction, two-point correlations of the streamwise velocity fluctuations in the spanwise direction for the range

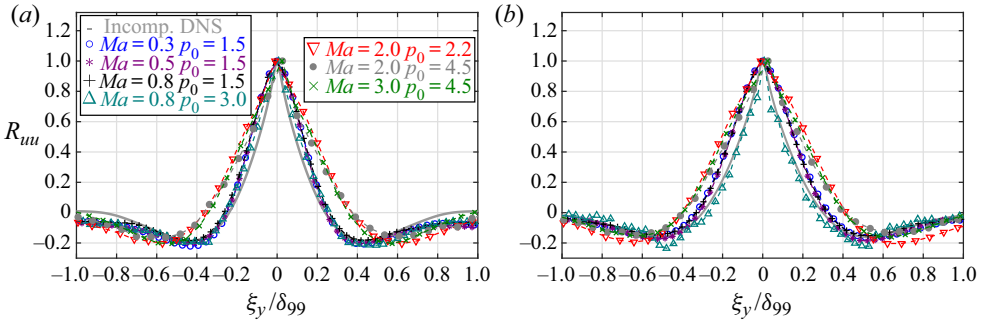

Figure 10. Two-point correlation coefficient R_{uu} slice across the spanwise direction at (*a*) $z_0/\delta_{99} = 0.2$ and (*b*) $z_0/\delta_{99} = 0.5$ for $0.3 \leq Ma \leq 3.0$. Plotted on the horizontal axis $\xi_y = y_0 + \Delta y$ where y_0 is the centre of the field of view in the spanwise direction and ξ_y is scaled with δ_{99}. Grey solid line represents incompressible reference R_{uu} from DNS computations at $Re_\tau \approx 2000$ or $Re_\theta \approx 6500$ (Sillero, Jiménez & Moser 2013) of a ZPG turbulent boundary layer.

of Mach and Reynolds numbers was done. Shown in figures 10(*a*) and 10(*b*) are slices of the correlation coefficient R_{uu} at $z_0/\delta_{99} = 0.2$ and 0.5. In these figures, the spanwise shift is represented as ξ_y, where $\xi_y = y_o + \Delta y$ with y_0 corresponding to the centre of the FOV in the spanwise direction.

The slices of R_{uu} at $z_0/\delta_{99} = 0.2$ interestingly reveal that there is a clear division between the correlations for $Ma < 1$ and the ones for $Ma > 1$. For $Ma < 1$ the distance between minimum correlation values is approximately $0.8\delta_{99}$, including the correlation result from a turbulent boundary layer incompressible DNS reference at $Re_\tau \approx 2000$ (Sillero *et al.* 2013). In contrast, for $Ma > 1$ the distance between minima is approximately $1.1\delta_{99}$, which is almost a 40 % increase from the subsonic cases. This implies that the spacing and or the width of superstructures increases rather discretely when the flow passes the sound barrier. Interestingly, this spacing increase appears to be independent of Mach number in the sense that no trend with Mach number is present except for the fact that the Mach number is either sub- or supersonic. Furthermore, the correlation is unaffected by Reynolds number since the correlations collapse for $Ma = 0.8$ $p_0 = 1.5$ and $p_0 = 3.0$ where Re_{δ_2} changes by a factor of two. The same collapse for the supersonic Reynolds number variation is also visible for $Ma = 2.0$ $p_0 = 2.2$ and $p_0 = 4.5$. A lack of the variation in the spanwise correlation length scales with Reynolds number was also confirmed in experimental investigations of incompressible turbulent boundary layers over several decades of Reynolds numbers in Hutchins & Marusic (2007*a*). If a slice of the correlation is taken at $z_0/\delta_{99} = 0.5$ as shown in figure 10(*b*), the discrete increase in spacing from $Ma < 1$ to $Ma > 1$ is still visible although width of correlations has increased when compared to the spacing at $z_0/\delta_{99} = 0.2$. In addition, the width increase of R_{uu} from subsonic to supersonic is only $\sim$20 % at this wall location.

The apparent discrepancy between the subsonic and supersonic correlation results cannot be explained by the relative change in scaled spatial resolution due to the change in boundary layer thickness, as shown in figure 11. For all Mach numbers the same physical spatial resolution, which is fixed by the size of the IW, was used. With an IW $= 24 \times 24$ pixels the smallest resolvable spatial scale for $Ma = 0.8$ $p_0 = 1.5$ is $0.018\delta_{99}$ and $0.035\delta_{99}$ for $Ma = 2.0$ $p_0 = 2.2$. To show that this variation in relative spatial resolution does not influence the correlation results, R_{uu} was calculated for different window size for $Ma = 0.8$ $p_0 = 1.5$ and $Ma = 2.0$ $p_0 = 2.2$ and is plotted in figure 11. For both the subsonic and supersonic cases a variation of IW size does not result in a change of the location of the

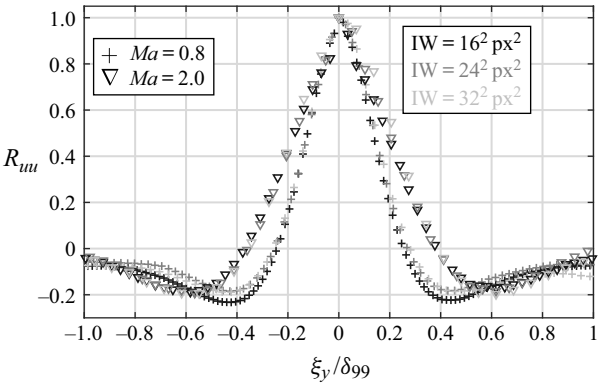

Figure 11. Two-point correlation coefficient R_{uu} slice across the spanwise direction at $z_0/\delta_{99} = 0.2$ of $Ma = 0.8$, $p_0 = 1.5$ and $Ma = 2.0$, $p_0 = 2.2$ for different minimum spatial resolutions based on the PIV interrogation window (IW) size. Plotted on the horizontal axis $\xi_y = y_0 + \Delta y$ where y_0 is the centre of the field of view in the spanwise direction and ξ_y is scaled with δ_{99}.

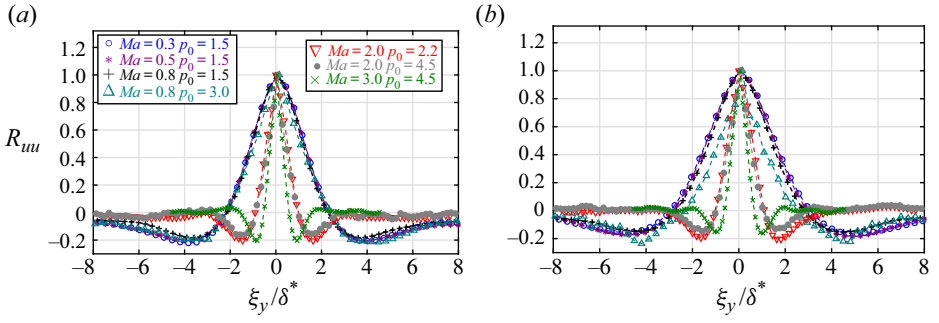

Figure 12. Two-point correlation coefficient R_{uu} slice across the spanwise direction at (*a*) $z_0/\delta_{99} = 0.2$ and (*b*) $z_0/\delta_{99} = 0.5$ for $0.3 \leq Ma \leq 3.0$. Plotted on the horizontal axis $\xi_y = y_0 + \Delta y$ where y_0 is the centre of the field of view in the spanwise direction and ξ_y is scaled with the displacement thickness δ^* (see (3.1)).

correlation peaks, which indicates that the spatial resolution of the presented measurement is sufficient to resolve the spacing of the superstructures in the spanwise direction when scaled with δ_{99}.

To demonstrate that the apparent bi-modal behaviour of structure spacing for the sub- and supersonic cases shown in figures 10(*a*) and 10(*b*) is influenced by the scaling, the same slices of R_{uu} are plotted in figures 12(*a*) and 12(*b*) except that ξ_y is scaled with the displacement thickness δ^*. Since the displacement thickness calculation in (3.1) depends on the mean density variation across the layer, a Mach number dependent variation in the δ^* scaled structure spacing, shown in figures 12(*a*) and 12(*b*), would be expected. Since δ^* increases with Mach number, see table 3, the structure spacing also decreases when scaled with δ^*. The bi-modal behaviour is still visible in the sense that there is a large jump in the structure spacing when the sound barrier is crossed to $Ma = 2$, but the spacing then continues to decrease up to $Ma = 3$. In any case, both the δ_{99} and δ^* scaling indicate that relative size or spacing of superstructures varies with Mach number. Since the majority of superstructure scales reported in the literature use δ_{99}, the following analysis will also use δ_{99} for scaling.

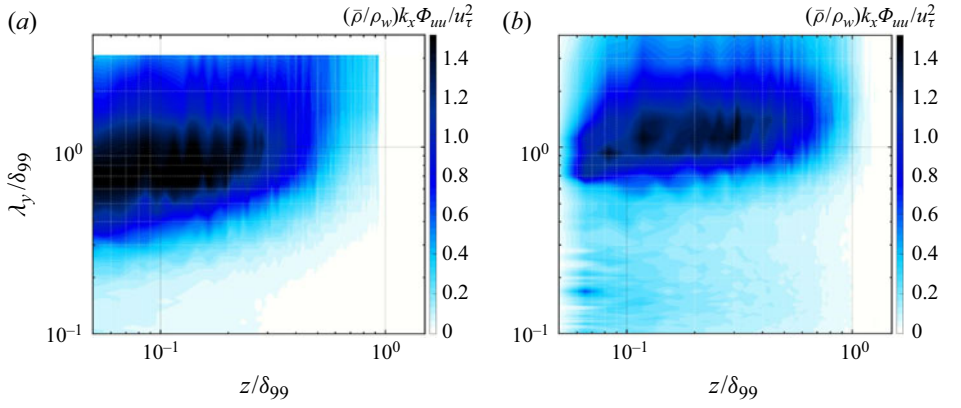

Figure 13. Pre-multiplied streamwise velocity spectrogram $(\bar{\rho}/\rho_w)k_y\Phi_{uu}/u_\tau^2$ for (*a*) $Ma = 0.3$, $p_0 = 1.5$ and (*b*) $Ma = 2.0$, $p_0 = 2.2$ as a function of spanwise wavelength, λ_y, and wall-normal direction, z, scaled with δ_{99}. The vertical and horizontal axis limits are the same in (*a*) as in (*b*).

To confirm these findings at different wall normal distances, the spectra of the streamwise velocity pre-multiplied with the spanwise wave number as a function of spanwise wave lengths and wall normal distance for $Ma = 0.3$, $p_0 = 1.5$ and $Ma = 2.0$, $p_0 = 2.2$ are plotted in figures 13(*a*) and 13(*b*). The *PSD* was computed from vector fields based on an interrogation window size of IW $= 24 \times 24$ pixels with 50 % overlap using in a similar way as in the previous section. The *PSD* was calculated for each wall-normal position along the entire extent of the streamwise distance for 1000 statistically independent velocity fields. The resolvable spanwise (λ_y) wavelength range calculated in the PSD spectrogram is from 0.5 mm to 81 mm.

The spectrograms plotted in figures 13(*a*) and 13(*b*) show both the wall-normal location and the spanwise wavelengths of spectral energy of streamwise velocity fluctuations in the cross-flow plane. The most energetic wavelengths for $Ma = 0.3$ vary between $\lambda_y = 0.7$ and $0.9\delta_{99}$, increasing slightly with wall-normal distance. Correspondingly, the most energetic wavelengths for $Ma = 2.0$ vary between $\lambda_y = 0.9$ and $1.2\delta_{99}$ with wall-normal distance. If these wavelengths are viewed as representative of the average spacing between two low- or high-momentum superstructures, the spectral results are consistent with the observations from the R_{uu} slices in figures 10(*a*) and 10(*b*). Therefore, it can be concluded that compressibility has a clear influence on the spanwise spacing scaled with δ_{99} of superstructures identified based on velocity fluctuations.

4.3. *Elongated structures in a wall parallel plane*

To confirm directly that long high- and low-momentum meandering superstructures exist in the log-law region for the subsonic and supersonic cases investigated herein, PIV measurements in a wall-parallel plane (xy) were performed. Two exemplary instantaneous fields of the fluctuating streamwise velocity normalized with the local mean velocity ($u'/\bar{u}$) are plotted in figures 14(*a*) and 14(*b*) for $Ma = 0.3$ $p_0 = 1.5$ and $Ma = 2.0$ $p_0 = 2.2$, respectively. The wall-parallel measurements were accomplished by aligning a laser light sheet parallel to the wall. Since the boundary layer thickness changes with Mach number, see table 3, the location of the measurement plane with respect to z/δ_{99} also changes with Mach number. Hence, the measurement plane was located at approximately $z/\delta_{99} = 0.1$ for the subsonic cases and at $z/\delta_{99} = 0.2$ for the supersonic cases. However, since both of

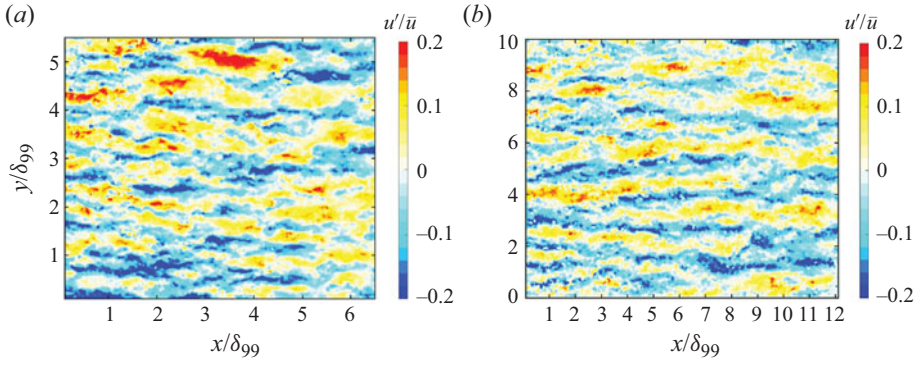

Figure 14. Instantaneous streamwise velocity fluctuation fields in the xy plane for (a) $Ma = 0.3$, $p_0 = 1.5$ and (b) $Ma = 2.0$, $p_0 = 2.2$. The measurement plane is located at $z/\delta_{99} = 0.1$ and 0.2 for $Ma = 0.3$ and 2.0, respectively.

these planes are located in the log-law layer, the presence of meandering superstructures in both the subsonic and supersonic cases is directly visible. Qualitatively, it can be seen that instantaneous high- and low-momentum structures can persist up to several boundary layer thicknesses and have a spanwise spacing of around one boundary layer thickness.

In the previous section, it was shown that the spatial correlations and spectral wavelengths associated with the spanwise spacing of the superstructures distinctly changes with Mach number. To confirm this finding in the wall-parallel plane, a spectral analysis of the streamwise velocity fluctuations in the spanwise direction was performed. Similar to the previous sections, a *PSD* was calculated for each streamwise location along the entire spanwise distance of the FOV and then averaged together to produce the plot shown in figure 15(a). In this plot, the peak in the spectra is located just below $\lambda_y/\delta_{99} = 1$ for both subsonic cases and slightly above $\lambda_y/\delta_{99} = 1$ for the supersonic cases. While the location of the wall-parallel measurement plane was at slightly different z/δ_{99} locations for the subsonic and supersonic cases due to the changing boundary layer thickness, the finding that the structure spacing is larger for supersonic as compared to subsonic is consistent with the finding in the previous section, i.e. see figures 13(a) and 13(b).

For incompressible flows it has been shown that the amount or intensity of spanwise meandering of individual superstructures increases with wall-normal height (Kevin, Monty & Hutchins 2019). Since the measurements shown in figure 15(a) are located at slightly different z/δ_{99} locations, a quantitative analysis of the meandering magnitude might be influenced by wall-normal measurement location rather than the Mach number variation. However, for the wall-normal locations 0.1 and $0.2\delta_{99}$ the meandering intensity variation is rather small (Kevin *et al.* 2019).

Instead of detecting individual structures and calculating their spanwise meandering frequency, the meandering influence on the spanwise length scale distribution for each Mach number can be deduced from a closer look at the spanwise spectra plotted in figure 15(a). The *PSD* is calculated for all streamwise locations in the spanwise direction and ensemble averaged over all velocity fields. Therefore, the resulting average spectra plotted in figure 15(a) contains all the measurable frequencies/wavelengths of the u' fluctuations in the spanwise direction. Since a distinct energetic peak of λ_y is visible for all Mach numbers, it can be concluded that there is only one structure (δ scaled) spacing or width present for each case. The distribution of the scales to the left and right of the maximum can then be related to the meandering nature of the superstructures. A more

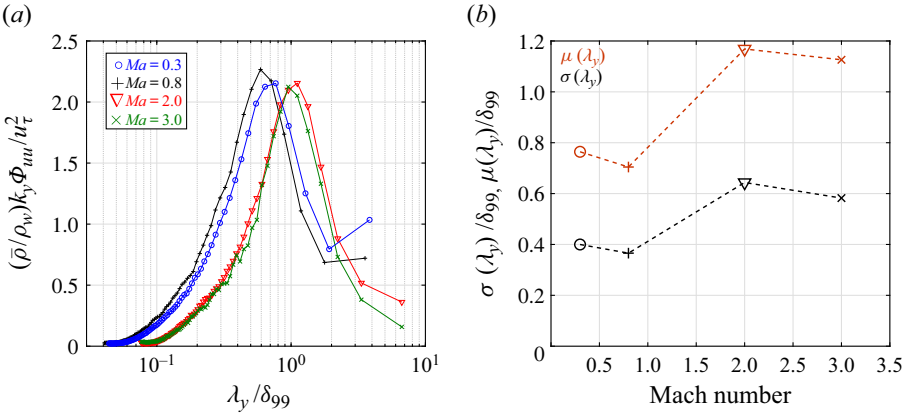

Figure 15. (*a*) Pre-multiplied streamwise velocity spectra $(\bar{\rho}/\rho_w)k_y\Phi_{uu}/u_\tau^2$ for $0.3 \leq Ma \leq 3.0$ vs. spanwise wavelength, λ_y scaled with δ_{99}. (*b*) Standard deviation σ and mean μ of a normal distribution fit of the spanwise wavelengths λ_y from (*a*) for each Mach number. Spectra calculated from wall-parallel planar PIV measurements.

narrow distribution of spanwise wavelengths would mean that the structures meander less than if a wider distribution were present.

To look at this point more carefully, a normal distribution was fitted to the spanwise wavelengths, λ_y, in figure 15(*a*). The standard deviation (σ) and mean (μ) of this fit for each Mach number in figure 15(*a*) are shown in figure 15(*b*). In addition to the peak λ_y value (μ) the width at 1σ is also larger for the supersonic cases. This would then imply that the meandering of the superstructures is also influenced by Mach number. However, the distinct shift in the spanwise wavelength of the most energetic fluctuations or μ from the fit also indicates that the average superstructure spacing or width is larger for the supersonic cases when scaled with δ_{99}.

5. Discussion and conclusions

In this work, ZPG turbulent boundary layers developing on a flat plate over a range of $0.3 \leq Ma \leq 3.0$ are measured with planar 2-D and stereo-PIV with the aim to study the characteristics of large-scale coherent structures otherwise known as superstructures. It is important to note that the comparison of subsonic, transonic and supersonic turbulent boundary layers is done in the same wind tunnel facility, where the flow quality is well documented for the range of Mach numbers considered (Scharnowski *et al.* 2019).

It was first shown that the organization of the flow field in the streamwise wall-normal direction remains qualitatively similar for sub- and supersonic cases. Elongated structures in the log-law layer with an inclination angle of $\sim 14^\circ$ in the instantaneous and mean correlation of streamwise velocity fluctuations were observed for both $Ma = 0.3$ and 2.0. In addition, 2–4 instantaneous UMZs in the log-law layer and wake region were detected for both cases, suggesting that the organization and layering of coherent motions are unchanged by Mach number.

In order to scale the mean velocity and fluctuations so that the mean variation of the density and temperature across the boundary layer are accounted for, a demonstration of the Van Driest and Morkovin scaling approaches were presented. The proper scaling was essential for the statistical analysis so that the sub- and supersonic flows can be compared. It was then demonstrated by using multi-point statistical and spatial

spectral methods applied to the data that compressibility has an effect on the spacing and spatial extent of superstructures in the streamwise and spanwise directions when scaled with δ_{99}. It was shown that superstructures in the sub- and supersonic boundary layers appear qualitatively similar to the incompressible cases found in the literature. However, the length, relative to the boundary layer thickness, of the streamwise energetic wavelengths associated with superstructures was shown to increase around 20 % from the subsonic to the supersonic case, which is in contrast to the decrease in streamwise mass flux $(\rho u)'$ correlation length with increasing Mach number reported in Smith & Smits (1995). Furthermore, while a slight increase in the streamwise correlation with increasing Mach number was shown herein, it was by far not as large of an increase (four times) as observed in Ganapathisubramani *et al.* (2006), which was also based on PIV measurements. The incompressible data compared in Ganapathisubramani *et al.* (2006) was an order of magnitude lower Reynolds number than the supersonic case, and therefore the large increase in the reported streamwise length scale could be partially explained by Reynolds number effects. For the comparison of streamwise length scales presented in this paper the Re_{δ_2} values for Mach 0.3 and 2.0 are almost identical.

Finally, the spanwise distribution of the superstructures were analysed and a distinct increase relative to the boundary layer thickness in the spanwise spacing of superstructures was observed for cases where $Ma > 1$ compared to the cases where $Ma < 1$. This was based on the two-point correlation and spectral calculations of the streamwise velocity fluctuations in the spanwise direction. A slight increase in spanwise spacing from subsonic to supersonic Mach number – around 15 % at $z/\delta = 0.5$ – was also noted in the DNS results of Pirozzoli & Bernardini (2011), which is similar to the results presented herein where the increase in spanwise spacing from subsonic to supersonic at $z/\delta_{99} = 0.5$ was $\sim$20 %. However, the aforementioned experimental investigations from the literature, either hot-wire or PIV, do not report a variation in the spanwise spacing with Mach number. The PIV measurements of Ganapathisubramani *et al.* (2006) actually show an increase in spanwise length scales when compared to an incompressible case at $z/\delta = 0.5$ but not at the $z/\delta = 0.1$ location, and the reported increase, much like the streamwise length scales, is much larger than both the results from DNS and the experiments presented herein.

There is not a definitive consensus on why there is a lack of agreement in the experimental results reported here and in the literature with regards to compressible flow structure length and spacing. However, a combination of different measurement techniques and facilities is likely a contributor, e.g. analysis of mass-flux $(\rho u)'$ and temperature fluctuations from hot-wire experiments versus only u' fluctuations recorded with PIV. The differences in PIV and hot-wire data might be simply explained by the fact that different quantities are measured. Furthermore, spatial scales from hot-wire measurements often rely on the validity of Taylor's frozen turbulence hypotheses whereas PIV offers the ability to measure the velocity distribution directly in a spatial domain. The applicability of hot-wires in compressible flow also depends on accurate calibrations, and the sensor itself must be robust enough to withstand the often harsh experimental conditions. However, recent developments in nano-scaled anemometer devices specially designed for compressible flows (Kokmanian *et al.* 2019) could be used to explore the turbulent dynamics of boundary layers in the future.

A downside of all these experimental techniques is that the instantaneous thermodynamic properties cannot be measured simultaneously or independently from the velocity field. While this is possible in DNS, numerical simulations are limited at the

moment to relatively low Reynolds numbers or to relatively small spatial and temporal domains making the convergence of statistics for large-scale structures difficult to achieve.

It is difficult to explain without speculating why other PIV results differ from the current data set results. For the measurements discussed herein, the comparisons between Mach numbers were performed in the same wind tunnel facility on the same boundary layer plate with the same measurement configurations. The wind tunnel operation and freestream properties are well documented in Scharnowski *et al.* (2019), and the corner vortices and leading edge transition details are also known. However the high Reynolds number range and other experimental features, e.g. the cold edge temperature for the supersonic case and the varying turbulence intensity in the freestream with Mach number, can make it challenging to compare to DNS.

Nevertheless, the experimental result presented herein does agree in part with the structural analysis in the available DNS. Therefore, it can be concluded that compressibility has a clear effect on boundary layer features and that the scaling of superstructures based on the boundary layer thickness results in longer and wider superstructures for supersonic turbulent boundary layers when compared to their subsonic counterparts. This result can be viewed as a challenge to Morkovin's assertion in 1962 'that the essential dynamics of these supersonic shear flows will follow the incompressible pattern'. However, assessing the complete physical details of these flows requires an independent measurement of all the fluctuating properties, i.e. velocity, density and temperature, in and around the flow structures, which is very challenging experimentally.

Funding. This work is supported by the Priority Programme SPP 1881 Turbulent Superstructures funded by the Deutsche Forschungsgemeinschaft project numbers KA1808/21-1 and KA1808/21-2.

Declaration of interests. The authors report no conflict of interest.

Author ORCIDs.
Matthew Bross http://orcid.org/0000-0003-4259-8090.

References

Adrian, R.J., Meinhart, C.D. & Tomkins, C.D. 2000 Vortex organization in the outer region of the turbulent boundary layer. *J. Fluid Mech.* **422**, 1–54.

Ames Research Staff 1953 Equations, tables and charts for compressible flow. *Tech. Rep.* 1135. NASA Tech. Report.

Baars, W.J., Hutchins, N. & Marusic, I. 2017 Reynolds number trend of hierarchies and scale interactions in turbulent boundary layers. *Phil. Trans. R. Soc.* A **375** (2089), 1–18.

Baidya, R., Scharnowski, S., Bross, M. & Kähler, C.J. 2020 Interactions between a shock and turbulent features in a Mach 2 compressible boundary layer. *J. Fluid Mech.* **893**, A15.

Balakumar, B.J. & Adrian, R.J. 2007 Large- and very-large-scale motions in channel and boundary-layer flows. *Phil. Trans. R. Soc.* A **365** (1852), 665–681.

Beresh, S.J., Clemens, N.T. & Dolling, D.S. 2002 Relationship between upstream turbulent boundary-layer velocity fluctuations and separation shock unsteadiness. *AIAA J.* **40** (12), 2412–2422.

Bradshaw, P. 1977 Compressible turbulent shear layers. *Annu. Rev. Fluid Mech.* **9** (1), 33–52.

Bross, M., Fuchs, T. & Kähler, C.J. 2019 Interaction of coherent flow structures in adverse pressure gradient turbulent boundary layers. *J. Fluid Mech.* **873**, 287–321.

Bross, M., Scharnowski, S. & Kähler, C.J. 2018 Influence of leading edge tripping devices on supersonic turbulent boundary layer characteristics. In *5th International Conference on Experimental Fluid Mechanics, July 2–4, Munich, Germany*.

Buchmann, N.A., Cierpka, C., Knopp, T., Schanz, D., Schröder, A., Hain, R. & Kähler, C.J. 2014 Large Scale Adverse Pressure Gradient Turbulent Boundary Layer Investigation by means of PIV and PTV. In *17th International Symposium on the Applications of Laser and Imaging Techniques to Fluid Mechanics, July 7–10, Lisbon, Portugal*.

BUCHMANN, N.A., KÜCÜKOSMAN, Y.C., EHRENFRIED, K. & KÄHLER, C.J. 2016 Wall pressure signature in compressible turbulent boundary layers. In *Progress in Wall Turbulence 2* (ed. M. Stanislas, J. Jimenez & I. Marusic), pp. 93–102. Springer International Publishing.

COLES, D. 1956 The law of the wake in the turbulent boundary layer. *J. Fluid Mech.* **1** (2), 191–226.

ELSINGA, G.E., ADRIAN, R.J., VAN OUDHEUSDEN, B.W. & SCARANO, F. 2010 Three-dimensional vortex organization in a high-Reynolds-number supersonic turbulent boundary layer. *J. Fluid Mech.* **644**, 35–60.

ELSINGA, G.E. & WESTERWEEL, J. 2012 Tomographic-PIV measurement of the flow around a zigzag boundary layer trip. *Exp. Fluids* **52** (4), 865–876.

FERNHOLZ, H.H. & FINLEY, P.J. 1980 A critical commentary on mean flow data for two-dimensional compressible turbulent boundary layers. In *AGARDograph 253*.

FERNHOLZ, H.H. & FINLEY, P.J. 1996 The incompressible zero-pressure-gradient turbulent boundary layer: an assessment of the data. *Prog. Aerosp. Sci.* **32** (4), 245–311.

GANAPATHISUBRAMANI, B., CLEMENS, N.T. & DOLLING, D.S. 2006 Large-scale motions in a supersonic turbulent boundary layer. *J. Fluid Mech.* **556**, 271–282.

GANAPATHISUBRAMANI, B., CLEMENS, N.T. & DOLLING, D.S. 2007 Effects of upstream boundary layer on the unsteadiness of shock-induced separation. *J. Fluid Mech.* **585**, 369–394.

GANAPATHISUBRAMANI, B., HUTCHINS, N., HAMBLETON, W.T., LONGMIRE, E.K. & MARUSIC, I. 2005 Investigation of large-scale coherence in a turbulent boundary layer using two-point correlations. *J. Fluid Mech.* **524**, 57–80.

GANAPATHISUBRAMANI, B., HUTCHINS, N., MONTY, J.P., CHUNG, D. & MARUSIC, I. 2012 Amplitude and frequency modulation in wall turbulence. *J. Fluid Mech.* **712**, 61–91.

HAIN, R., KÄHLER, C.J. & RADESPIEL, R. 2009 Dynamics of laminar separation bubbles at low-Reynolds-number aerofoils. *J. Fluid Mech.* **630**, 129–153.

HOPKINS, E.J. & INOUYE, M. 1971 An evaluation of theories for predicting turbulent skin friction and heat transfer on flat plates at supersonic and hypersonic mach. *AIAA J.* **9**, 993–1003.

HUTCHINS, N. 2012 Caution: tripping hazards. *J. Fluid Mech.* **710**, 1–4.

HUTCHINS, N. & MARUSIC, I. 2007*a* Evidence of very long meandering features in the logarithmic region of turbulent boundary layers. *J. Fluid Mech.* **579**, 1–29.

HUTCHINS, N. & MARUSIC, I. 2007*b* Large-scale influences in near-wall turbulence. *Phil. Trans. R. Soc.* A **365**, 647–664.

HUTCHINS, N., MONTY, J.P., GANAPATHISUBRAMANI, B., NG, H.C.H. & MARUSIC, I. 2011 Three-dimensional conditional structure of a high-Reynolds-number turbulent boundary layer. *J. Fluid Mech.* **673**, 255–285.

KÄHLER, C.J., SAMMLER, B. & KOMPENHANS, J. 2002 Generation and control of tracer particles for optical flow investigations in air. *Exp. Fluids* **33**, 736–742.

VON KÁRMÁN, T. 1934 Turbulence and skin friction. *J. Aero. Sci.* **1**, 1–20.

KEVIN, K., MONTY, J. & HUTCHINS, N. 2019 The meandering behaviour of large-scale structures in turbulent boundary layers. *J. Fluid Mech.* **865**, R1.

KLINE, S.J., REYNOLDS, W.C., SCHRAUB, F.A. & RUNSTADLER, P.W. 1967 The structure of turbulent boundary layers. *J. Fluid Mech.* **30**, 741–773.

KOKMANIAN, K., SCHARNOWSKI, S., BROSS, M., DUVVURI, S., FU, M.K., KÄHLER, C.J. & HULTMARK, M. 2019 Development of a nanoscale hot-wire probe for supersonic flow applications. *Exp. Fluids* **60** (10), 150.

KOVASZNAY, L.S.G. 1953 Turbulence in supersonic flow. *J. Aero. Sci.* **20** (10), 657–674.

KOVASZNAY, L.S.G., KIBENS, V. & BLACKWELDER, R.F. 1970 Large-scale motion in the intermittent region of a turbulent boundary layer. *J. Fluid Mech.* **41** (2), 283–325.

LASKARI, A., DE KAT, R., HEARST, R.J. & GANAPATHISUBRAMANI, B. 2018 Time evolution of uniform momentum zones in a turbulent boundary layer. *J. Fluid Mech.* **842**, 554–590.

MARUSIC, I., CHAUHAN, K.A., KULANDAIVELU, V. & HUTCHINS, N. 2015 Evolution of zero-pressure-gradient boundary layers from different tripping conditions. *J. Fluid Mech.* **783**, 379–411.

MARUSIC, I. & HEUER, W.D.C. 2007 Reynolds number invariance of the structure inclination angle in wall turbulence. *Phys. Rev. Lett.* **99**, 114504.

MEINHART, C.D. & ADRIAN, R.J. 1995 On the existence of uniform momentum zones in a turbulent boundary layer. *Phys. Fluids* **7**, 694–696.

MONTY, J.P., HUTCHINS, N., NG, H.C.H., MARUSIC, I. & CHONG, M.S. 2009 A comparison of turbulent pipe, channel and boundary layer flows. *J. Fluid Mech.* **632**, 431–442.

MORKOVIN, M.V. 1962 Effects of compressibility on turbulent flows. In *Mecanique de la Turbulence* (ed. A. Favre). CNRS.

PIROZZOLI, S. & BERNARDINI, M. 2011 Turbulence in supersonic boundary layers at moderate Reynolds number. *J. Fluid Mech.* **688**, 120–168.

RAFFEL, M., WILLERT, C., SCARANO, F., KÄHLER, C.J., WERELEY, S.T. & KOMPENHANS, J. 2018 *Particle Image Velocimetry: A Practical Guide*. Springer.

RAGNI, D., SCHRIJER, F., VAN OUDHEUSDEN, B.W. & SCARANO, F. 2011 Particle tracer response across shocks measured by PIV. *Exp. Fluids* **50** (1), 53–64.

REUTHER, N. & KÄHLER, C.J. 2018 Evaluation of large-scale turbulent/non-turbulent interface detection methods for wall-bounded flows. *Exp. Fluids* **59**, 121.

RINGUETTE, M.J., WU, M. & MARTÍN, M.P. 2008 Coherent structures in direct numerical simulation of turbulent boundary layers at Mach 3. *J. Fluid Mech.* **594**, 59–69.

SAMIE, M., MARUSIC, I., HUTCHINS, N., FU, M.K., FAN, Y., HULTMARK, M. & SMITS, A.J. 2018 Fully resolved measurements of turbulent boundary layer flows up to $Re_\tau = 20\,000$. *J. Fluid Mech.* **851**, 391–415.

SANMIGUEL VILA, C., VINUESA, R., DISCETTI, S., IANIRO, A., SCHLATTER, P. & ÖRLÜ, R. 2017 On the identification of well-behaved turbulent boundary layers. *J. Fluid Mech.* **822**, 109–138.

SCHARNOWSKI, S., BROSS, M. & KÄHLER, C.J. 2019 Accurate turbulence level estimations using PIV/PTV. *Exp. Fluids* **60** (1), 1.

SCHOENHERR, K.E. 1932 Resistance of flat surfaces moving through a fluid. *S. Nav. Arch. Mar. Engng* **40**, 273–313.

SCIACCHITANO, A. 2019 Uncertainty quantification in particle image velocimetry. *Meas. Sci. Technol.* **30** (9), 092001.

SILLERO, J.A., JIMÉNEZ, J. & MOSER, R.D. 2013 One-point statistics for turbulent wall-bounded flows at Reynolds numbers up to $\delta^+ \approx 2000$. *Phys. Fluids* **25** (10), 105102.

DE SILVA, C.M., HUTCHINS, N. & MARUSIC, I. 2016 Uniform momentum zones in turbulent boundary layers. *J. Fluid Mech.* **786**, 309–331.

DE SILVA, C.M., KEVIN, K., BAIDYA, R., HUTCHINS, N. & MARUSIC, I. 2018 Large coherence of spanwise velocity in turbulent boundary layers. *J. Fluid Mech.* **847**, 161–185.

DE SILVA, C.M., PHILIP, J., HUTCHINS, N. & MARUSIC, I. 2017 Interfaces of uniform momentum zones in turbulent boundary layers. *J. Fluid Mech.* **820**, 451–478.

SMITH, M.W. & SMITS, A.J. 1995 Visualization of the structure of supersonic turbulent boundary layers. *Exp. Fluids* **18** (4), 288–302.

SMITS, A.J. & DUSSAUGE, J.P. 2006 *Turbulent Shear Layers in Supersonic Flow*. Springer.

SMITS, A.J., MATHESON, N. & JOUBERT, P.N. 1983 Low-Reynolds-number turbulent boundary layers in zero and favorable pressure gradients. *J. Ship Res.* **27** (3), 147–157.

SMITS, A.J., SPINA, E.F., ALVING, A.E., SMITH, R.W., FERNANDO, E.M. & DONOVAN, J.F. 1989 A comparison of the turbulence structure of subsonic and supersonic boundary layers. *Phys. Fluids* A **1** (11), 1865–1875.

SPINA, E.F., DONOVAN, J.F. & SMITS, A.J. 1991 On the structure of high-Reynolds-number supersonic turbulent boundary layers. *J. Fluid Mech.* **222**, 293–327.

SUTHERLAND, W. 1883 The viscosity of gases and molecular force. *Phil. Mag. Ser. 5* **36** (223), 507–531.

TAYLOR, G.I. 1938 The spectrum of turbulence. *Proc. R. Soc.* A **164** (919), 476–490.

VAN DRIEST, E.R. 1951 Turbulent boundary layer in compressible fluids. *J. Aero. Sci.* **18**, 145–160.

VAN DRIEST, E.R. 1956 On turbulent flow near a wall. *J. Aero. Sci.* **23**, 1007–1011.

WALLACE, J.M. 2012 Highlights from 50 years of turbulent boundary layer research. *J. Turbul.* **13**, 1–70.

WALZ, A. 1966 *Strömungs- und Temperaturgrenzschichten*. Braun Verlag, Karlsruhe, English translation *Boundary Layers of Flow and Temperature*, MIT Press, 1969.

WELCH, P.D. 1967 The use of fast fourier transform for the estimation of power spectra: a method based on time averaging over short, modified periodograms. *IEEE Trans. Audio Electroacoust.* **15** (2), 70–73.

WENZEL, C., SELENT, B., KLOKER, M. & RIST, U. 2018 DNS of compressible turbulent boundary layers and assessment of data/scaling-law quality. *J. Fluid Mech.* **842**, 428–468.

WILLIAMS, O.J.H., SAHOO, D., BAUMGARTNER, M.L. & SMITS, A.J. 2018 Experiments on the structure and scaling of hypersonic turbulent boundary layers. *J. Fluid Mech.* **834**, 237–270.